

1
2
3
4
5
6
7
8
9
10
11
12
13
14
15
16
17
18

**Impacts of Arctic sea-ice and continental snow-cover changes
on atmospheric winter teleconnections**

Dörthe Handorf, Ralf Jaiser, Klaus Dethloff, Annette Rinke, Judah Cohen

Dörthe Handorf, Ralf Jaiser, Klaus Dethloff, and Annette Rinke, Alfred Wegener Institute,
Helmholtz Center for Polar and Marine Research, Research Unit Potsdam, Potsdam,
Germany.

Judah Cohen, Atmospheric and Environmental research, Inc., Lexington, Massachusetts
02421, USA

Corresponding author: D. Handorf, Alfred Wegener Institute, Helmholtz Center for Polar and
Marine Research, Research Unit Potsdam, Telegrafenberg A43, D-14473 Potsdam, Germany.
(doerthe.handorf@awi.de)

19 KEY POINTS

20 • Changes in Arctic sea ice and Northern Hemisphere snow cover in autumn induce a negative
21 Arctic Oscillation in winter and a strengthening and westward shift of the Siberian High

22 • The observed negative Arctic Oscillation in winter in response to changes in sea ice and
23 snow cover in autumn is too weakly reproduced by a state-of-the-art global atmospheric
24 model

25 • Deficits in the model simulated planetary wave propagation characteristics in response to
26 sea-ice and snow-cover changes are identified

27 ABSTRACT

28 Extreme winters in Northern Hemisphere mid-latitudes in recent years have been connected to
29 declining Arctic sea ice and continental snow-cover changes in autumn following modified
30 planetary waves in the coupled troposphere-stratosphere system. Through analyses of
31 reanalysis data and model simulations with a state-of-the-art atmospheric general circulation
32 model we investigate the mechanisms between Arctic Ocean sea ice and Northern
33 Hemisphere land snow-cover changes in autumn and atmospheric teleconnections in the
34 following winter. The observed negative Arctic Oscillation in response to sea-ice cover
35 changes is too weakly reproduced by the model. The planetary wave train structures over the
36 Pacific and North America region are well simulated. The strengthening and westward shift of
37 the Siberian high pressure system in response to sea-ice and snow-cover changes is
38 underestimated compared to ERA-Interim data due to deficits in the simulated changes in
39 planetary wave propagation characteristics.

40

41 INDEX TERMS AND KEYWORDS

42 Index terms: climate change and variability, stratosphere/troposphere interaction, sea ice,
43 snow

44 Keywords: polar-mid-latitude linkages, planetary wave activity, cold Eurasian winters

45

46 **1. Introduction**

47 The Arctic is on the track to a new climate regime dominated by thinner first-year ice [*Kwok*
48 *and Rothrock, 2009*]. The decline in Arctic summer sea-ice concentration is connected with
49 atmospheric circulation responses in the following winter months [*Cohen et al., 2014; Liu et*
50 *al., 2012; Mori et al., 2014; Overland and Wang, 2010; Overland et al., 2011; Vihma, 2014*]
51 and linked to anomalous cold winters over Eurasia [*Honda et al., 2009; Cohen et al., 2014;*],
52 and other regions of the Northern Hemisphere [*Cohen et al., 2014; Francis et al., 2009*]. Sea-
53 ice decline leads to an enhanced absorption of solar radiation in the mixed layer of the Arctic
54 Ocean in autumn and intensifies the vertical fluxes of heat and moisture into the atmosphere.
55 This can be seen in model results and reanalysis data [e.g., *Rinke et al., 2013; Screen and*
56 *Simmonds, 2010; Kim et al., 2014*]. As shown by *Sato et al. [2014]* horizontal advection of
57 heat and moisture can reduce the strength of vertical latent and sensible heat fluxes. Since
58 there are no in-situ measurements of vertical latent and sensible heat fluxes available reliable
59 trends in these fluxes following sea ice decline can not be estimated as discussed by *Boisvert*
60 *et al. [2013]*. Through reduced vertical stability, baroclinic systems grow in autumn and exert
61 a strong impact on the intensification of planetary waves in the coupled troposphere-
62 stratosphere system in the following winter [*Jaiser et al., 2012*]. Eliassen-Palm fluxes [*Jaiser*
63 *et al., 2012, 2013; Trenberth, 1986*] due to planetary waves are enhanced as a result of the

64 stronger diabatic heat source associated with the larger open ocean areas when Arctic sea ice
65 is low. The enhanced baroclinic systems and modified cloud development processes impact
66 the hydrological cycle and snowfall over the continental areas [Park *et al.*, 2013; Ghatak *et*
67 *al.*, 2010]. Therefore in addition to sea-ice changes, associated snow-cover changes affect the
68 winter large-scale atmospheric circulation [Cohen *et al.*, 2013]. Interactions between
69 baroclinic processes and large-scale planetary wave changes trigger a negative surface Arctic
70 Oscillation (AO) signal that extends up to the stratosphere in winter, which is connected to
71 reduced sea-ice cover in late summer [Kim *et al.*, 2014; Jaiser *et al.*, 2013]. Another process
72 impacting the winter AO signal is related to Siberian snow cover anomalies in October.
73 Though the satellite data [Robinson *et al.*, 1993] exhibits a positive trend in October snow
74 cover, Brown and Derksen [2013] found a negative trend using reanalysis data, in-situ snow
75 depth observations and passive microwave data. Despite this observational uncertainty in the
76 trend of October snow extent, positive anomalies of Siberian snow cover in October enhance
77 planetary wave activity resulting in a negative winter AO signal [Cohen *et al.*, 2007, 2012;
78 Allen and Zender, 2011]. The sea-ice related and snow-cover related mechanisms are
79 connected through changed moisture budgets following the Arctic sea-ice decline [Cohen *et*
80 *al.*, 2012]. Low sea ice and extensive snow cover, by influencing the characteristics of
81 baroclinic cyclones and the AO pattern, modify the exchange of heat and moisture between
82 the warmer ocean and the atmosphere [Kim *et al.*, 2014; Cohen *et al.*, 2012; Orsolini *et al.*,
83 2012; Sokolova *et al.*, 2007].

84 Here we investigate the relationships between the recent Arctic sea-ice decline and snow-
85 cover changes over the continental land areas with atmospheric circulation changes on the
86 basis of one of the most reliable reanalysis data set from 1979-2012 (ERA-Interim) [Dee *et*
87 *al.*, 2004]. We compare the reanalysis data with ensemble simulations of the atmospheric
88 general circulation model (AGCM) ECHAM6 [Stevens *et al.*, 2013] from 1979-2008 to check

89 whether a state-of-the-art AGCM is able to reproduce the observed relationships. To
90 understand the differences in the observed and simulated atmospheric circulation response in
91 winter following sea-ice and snow-cover anomalies in autumn, the wave activity in the
92 troposphere and the stratosphere has been diagnosed similar to *Jaiser et al.* [2012, 2013] and
93 *Sokolova et al.* [2007].

94 **2. Data and Methodology**

95 **2.1 Data and model simulations**

96 We used observed monthly sea-ice concentration fields from the Hadley Centre Sea Ice and
97 Sea Surface Temperature (HadISST) data set [*Rayner et al.*, 2003; [www.metoffice.gov.uk/
98 hadobs/hadisst/](http://www.metoffice.gov.uk/hadobs/hadisst/)], and observed monthly snow cover fields from Rutgers University snow data
99 set [*Robinson et al.*, 1993; <http://climate.rutgers.edu/measures/snowice/>]. The sea-ice index,
100 defined as monthly mean sea-ice extent has been provided by the National snow and ice data
101 center [*Fetterer and Knowles*, 2004; [ftp://sidacs.colorado.edu/DATASETS/NOAA/G02135
102 /Sep/N_09_area.txt](ftp://sidacs.colorado.edu/DATASETS/NOAA/G02135/Sep/N_09_area.txt)]. Based on this sea-ice index for September we defined the time period
103 1979-1999 as high-ice phase. The time period 2000-2012 with considerably smaller mean
104 values of sea-ice extent is referred to as low-ice phase. Atmospheric reanalysis data ERA-
105 Interim have been obtained from the European Centre for Medium-range Weather Forecasts
106 [*Dee et al.*, 2004; <http://apps.ecmwf.int/datasets/>].

107 The ensemble simulations of the AGCM ECHAM6 [*Stevens et al.*, 2013] have been
108 performed by the Coupled Model Intercomparison Project Phase 5 (CMIP5) project [*Taylor et
109 al.*, 2012] as part of the CMIP5 Atmospheric Model Intercomparison Project (AMIP)
110 simulations. The analyzed ensemble simulations are available from the CMIP5 archive
111 (<http://cmip-pcmdi.llnl.gov/cmip5/>). The model simulations have been performed over the
112 period from 1979 to 2008 with a horizontal spectral resolution of T63 (approximately 2

113 degree in longitude and latitude) and 96 vertical levels up to 0.01 hPa (about 80 km). At the
114 lower boundary the atmospheric model is driven by observed mid-month sea-surface
115 temperature and sea-ice concentration data that is linearly interpolated to obtain daily forcing
116 values [Hurrell *et al.*, 2008; [http://www-pcmdi.llnl.gov/projects/amip/AMIP2EXPDSN/BCS/
117 amipobs_dwnld.php](http://www-pcmdi.llnl.gov/projects/amip/AMIP2EXPDSN/BCS/amipobs_dwnld.php)]. The analyzed ensemble comprises of three members. All results are
118 described with regard to the ensemble mean for each season, year and period, respectively.

119 **2.2 Statistical and dynamical analysis**

120 The statistical relation between fields of sea-ice concentration or snow cover and atmospheric
121 data is analyzed using a maximum covariance analysis (MCA) [von Storch and Zwiers, 1999].
122 Prior to the MCA, each field has been detrended by removing the long-term linear trend. The
123 MCA results in pairs (MCA modes) of spatial patterns and associated time series for each
124 field, which are coupled through a maximized covariance of their associated time series. For
125 each MCA mode, the spatial patterns are shown as regression maps determined by regressing
126 both data fields (sea-ice concentration or snow cover and atmospheric fields) of the MCA
127 onto the same standardized associated time series for the atmospheric field for the respective
128 MCA mode. Therefore, the regression maps for the atmospheric fields are called
129 homogeneous regression maps, whereas the regression maps for the sea-ice concentration or
130 snow cover fields are called heterogeneous regression maps. The regression maps represent
131 typical anomaly patterns associated with the MCA. Statistical significance of the regression
132 maps is determined by applying a two-tailed Student's t-test for correlation at 95% confidence
133 level.

134 The localized Eliassen Palm fluxes (EP flux) have been computed [see Jaiser *et al.*, 2013;
135 Trenberth, 1986; Cohen *et al.*, 2007] to diagnose the wave activity in the troposphere and the
136 stratosphere. For the calculation of flux terms not influenced by the seasonal trends the

137 seasonal cycle has been removed. To consider the changes in synoptic-scale and planetary-
138 scale fluxes separately, two digital filters are used [*Blackmon and Lau, 1980*]. Synoptic-scale
139 fluctuations are extracted by a band-pass filter sensitive to time periods between 2.5 and 6
140 days. Periods longer than 10 days known as planetary-scale fluctuations have been filtered
141 with a low-pass filter. Statistical significance of correlations of magnitude of EP-flux vectors
142 with sea-ice and snow-cover indices is assessed using a two-tailed Student's t-test for
143 correlation at 90% and 95% confidence level. Furthermore, differences in magnitude of EP-
144 flux vectors between the time periods are investigated for significance using a Mann-
145 Whitney-Wilcoxon test with 90% and 95% confidence level.

146 **3. Results and discussions**

147 By applying a MCA, optimized coherent large-scale patterns of September sea-ice
148 concentration and October snow-cover extent have been detected, which covary with the
149 atmospheric circulation structures in the following winter. Fig. 1 displays the first pair of
150 coupled MCA patterns of Arctic sea-ice concentration in September (HadISST monthly mean
151 data) with ERA-Interim fields of sea-level pressure (SLP), 500 hPa and 50 hPa geopotential
152 height fields (GPH500 and GPH50) in winter (DJF mean) for the period 1979-2012. The
153 leading MCA patterns explain 44%, 32% and 56% (for SLP, GPH500 and GPH50) of the
154 squared covariance fraction. At all levels, the leading MCA mode describes diminishing sea
155 ice over the northern edge of the Barents Sea, the Kara, Laptev and Chukchi and Beaufort
156 Seas covarying with a pressure anomaly pattern resembling the negative phase of the AO
157 throughout the troposphere and stratosphere with a predominantly zonally symmetric
158 response. In the troposphere this mode leads to a weakened Icelandic Low and a westward
159 shifted and strengthened Siberian High.

160 There is a statistical connection between September sea-ice anomalies over the Arctic and
161 November sea-ice anomalies in the Barents and Kara Sea. This sea-ice decline in November
162 could be connected with warm southerly advection induced by the poleward shift of the
163 baroclinic zone over the Gulf Stream as stated by *Sato et al.* [2014]. As pointed out by *Jaiser*
164 *et al* [2013], the September sea-ice anomaly forces a negative AO response via barotropic-
165 baroclinic interactions, whereas the November ice anomaly directly changes the planetary
166 wave train as suggested by *Honda et al.* [2009] and *Sato et al.* [2014]. *Jaiser et al.* [2013]
167 prioritizes the importance of vertical heat and moisture fluxes in September, whereas *Sato et*
168 *al.* [2014] assume that meridional flux advection in early winter is the main trigger for the
169 wave train changes.

170 The second most important pairs of coupled MCA patterns between the sea-ice concentration
171 field and atmospheric fields of SLP, GPH500 and GPH50 (Fig. 2) explain 18%, 21% and 11%
172 of the squared covariance fraction, respectively. In the troposphere, a September sea-ice
173 pattern with sea-ice retreat over the Beaufort Sea and over the East Siberian Sea and northern
174 Barents and Kara Seas is preceding a more wavelike atmospheric response. At the surface, the
175 SLP anomaly pattern is characterized by an enhanced pressure anomaly westward of the
176 Aleutian Low in the North Pacific and northward shift of the Icelandic Low. Over Eurasia a
177 positive circulation anomaly appears which again contributes to a westward shifted and
178 strengthened Siberian High. At 500 hPa, the atmospheric anomaly pattern shows distinct
179 similarity with the surface anomaly pattern. In the stratosphere, a wavenumber-one pattern
180 indicating a shift of the polar vortex towards Canada and Alaska that is related to sea-ice
181 retreat over the Beaufort Sea and northern Kara Sea.

182 Fig. 3 displays the leading MCA patterns of Arctic sea-ice concentration in September
183 (HadISST data) with the ECHAM6 ensemble mean fields of SLP, GPH500 and GPH50 in
184 winter for the period 1979-2008. The MCA modes explain 38%, 37% and 51% (for SLP,

185 GPH500 and GPH50) of the squared covariance fraction. In the troposphere, the leading
186 MCA patterns bear resemblance with the second MCA patterns from the reanalysis data (Fig.
187 2). That means, September sea-ice retreat over the Beaufort and the East Siberian Seas
188 precedes an atmospheric wave-train response over the Pacific and North America. Over the
189 North Atlantic, a northward shift of the Icelandic Low is detected. The centers of action of the
190 atmospheric patterns are stronger over the Pacific region than over the Atlantic region and the
191 observed westward shifted and strengthened Siberian High is not simulated. In the
192 stratosphere a weak wavenumber-one pattern, related to sea-ice decline in the Laptev Sea
193 appears, with a shift of the polar vortex towards Canada. The model indicates in the second
194 MCA mode (not shown) changes in the Siberian high pressure system in accordance with
195 observations connected to sea-ice reduction over the Beaufort Sea and a partly reproduction of
196 the observed negative AO pattern.

197 By applying an MCA to the Northern Hemisphere snow cover based on the Rutgers
198 University snow data set for October from 1979-2012 [*Robinson et al.*, 1993] and the ERA-
199 Interim SLP and GPH500 fields in winter (DJF mean for the period 1979-2012), again a
200 quasi-barotropic atmospheric response pattern with zonally symmetric character is detected
201 and displayed in Fig. 4. These coupled patterns explain 45% and 39% of the squared
202 covariance. A pattern of enhanced snow cover over Canada, Scandinavia, northern European
203 Russia and the southern part of Siberia is related to pressure anomaly patterns resembling the
204 negative phase of the AO.

205 As for the reanalysis data, an MCA was also applied to the fields of Northern Hemisphere
206 snow-cover distribution for October with ECHAM6 ensemble mean fields of SLP and
207 GPH500 in winter (DJF mean). The snow cover fields have been taken as the ensemble mean
208 of the October snow cover simulated by ECHAM6. The leading pair of MCA patterns
209 (Supplementary Fig. S1) between simulated snow-cover anomalies and simulated atmospheric

210 fields of SLP and GPH500 explain 26% and 30% of the squared covariance fraction which is
211 less than in the reanalysis data. The snow-cover changes of the leading mode display
212 increases over large parts of eastern Siberia and northwest America and decrease over west
213 Siberia and eastern North America. The structure and amplitude of this pattern is different
214 compared to those obtained by the MCA with the reanalysis data, which suggests differences
215 between the simulated and observed snow cover. The related atmospheric response fields of
216 this leading mode are characterized by quasi-barotropic wave structures and bear a strong
217 similarity with the simulated leading atmospheric patterns related to sea-ice changes (compare
218 Fig. S1 and Fig. 3).

219 The model underestimates the strong negative AO response to sea ice and snow cover
220 anomalies detected in the reanalysis data. To understand the origin of these model
221 shortcomings in the atmospheric circulation response in winter following sea-ice and snow-
222 cover anomalies in autumn, the wave activity in the troposphere and the stratosphere has been
223 diagnosed [*Jaiser et al.*, 2012, 2013; *Sokolova et al.*, 2007]. The localized Eliassen-Palm (EP)
224 flux vectors [*Trenberth*, 1986] (see methods) have been calculated for baroclinic-scale waves
225 (timescale of 2.5-6 days) and for planetary-scale waves (timescale of 10-90 days).

226 Fig. 5a displays the correlation of the September sea-ice index with the zonally averaged
227 magnitude of planetary-scale EP flux vector in winter calculated from reanalysis data over the
228 period 1979-2012. Reduced sea ice is connected with enhanced EP fluxes in the whole
229 troposphere and lower stratosphere northward of ca 50°N. The corresponding correlations
230 between the zonally averaged magnitude of planetary-scale EP flux vector in winter with the
231 September sea-ice index for the ECHAM6 simulations over the period 1979-2008 are shown
232 in Fig. 5c. In accordance with the reanalysis data enhanced planetary-scale EP fluxes in the
233 troposphere and stratosphere are related to reduced sea ice, but the latitudinal belt of

234 significant correlations is shifted to the south, and no significant signals are detected over the
235 polar regions north of 60°N.

236 Similar correlation analyses have been performed for an October snow-cover index (defined
237 as area average of snow cover over 0°-190°E, 50°-90°N, based on the Rutgers University
238 snow dataset). Based on reanalysis data the correlations between the snow-cover index and
239 the magnitude of EP fluxes are positive in the whole tropospheric polar cap connecting
240 enhanced snow cover to increased EP fluxes (see Fig. 5b). The comparison of Figs. 5a and 5b
241 gives hints on a vertically more extended impact of sea-ice anomalies on the planetary wave
242 fluxes in winter compared to the impact of snow-cover anomalies. The correlations between
243 zonally averaged magnitudes of planetary-scale EP flux vectors in winter with the simulated
244 October snow-cover index (defined as area average of snow cover over 0°-190°E, 50°-90°N)
245 over the period 1979-2008 for the ECHAM6 ensemble are shown in Fig. 5d. In contrast to the
246 results for the reanalysis data (Fig. 5b), the model simulations do not reveal statistically
247 significant correlations. The modelled snow-cover impact is weaker relative to the
248 observations and suggests deficits in the coupled atmosphere-snow-soil feedbacks over land
249 which impacts on the wave propagation from the surface into the stratosphere.

250 The impact of tropospheric changes following variability in autumn sea ice and snow cover
251 onto the overlying stratosphere is determined by the troposphere-stratosphere coupling and is
252 studied in terms of the related changes in the activity and propagation of planetary-scale
253 waves. The winter climatology (i.e. the long-term average over the winters 1979-2012) of the
254 zonally averaged magnitude of the planetary-scale EP-fluxes for the ERA-Interim data is
255 shown in supplementary Figs. S2a and S2b separately for the Atlantic Ocean sector (average
256 over 60°W-30°E) and the Pacific Ocean sector (average over 150°E-240°E). The maxima in
257 the upper troposphere at about 50°N (Atlantic sector) and at about 35°N (Pacific sector) are
258 related to the eddy-driven jets, which are located at these positions. At the tropopause level,

259 the EP fluxes have a local minima and their magnitude increases with height throughout the
260 lower and middle stratosphere.

261 The changes between low-ice (2001-2012) and high-ice (1979-2000) phases for the reanalysis
262 data display large differences between the two ocean basins (Supplementary Figs. S2c and
263 S2d). Over the Atlantic sector (Fig. S2c), strong, significant changes of the magnitudes of the
264 planetary-scale EP-fluxes are found between 45°N-70°N in the lower and middle troposphere,
265 which are mainly due to an increase in the vertical component of the wave flux. Above 300
266 hPa, the increase in the EP flux in the mid-latitudes is due to stronger southward wave fluxes.
267 The increase in stratospheric fluxes is mainly determined by the enhanced vertical component
268 of the wave fluxes. Over the Pacific (Fig. S2d), the corresponding difference plot between
269 low-ice and high-ice phases is characterized by negative values, except in the troposphere
270 over the polar region. The negative differences of the magnitude of the planetary-scale EP-
271 fluxes in the stratosphere up to 10 hPa and in the mid-latitude troposphere are mainly due to a
272 weakening of the upward component of the wave flux.

273 The ECHAM6 ensemble mean climatology of the zonally averaged magnitude of the
274 planetary-scale EP-fluxes (shown in Supplementary Figs. S3a and S3b) shows good
275 agreement with the ERA-Interim results, in particular the tropospheric maxima are located at
276 similar latitudes. Despite this agreement, the corresponding difference plots between low-ice
277 and high-ice phases differ with those obtained from the reanalysis data. Over the Atlantic
278 sector (Fig. S3c) decreased vertical wave fluxes cause negative differences throughout the
279 troposphere from 20°N to 80°N. The observed increase in the stratospheric wave fluxes (cf.
280 Fig. S2c) is only partly reproduced with differences in the location of the maximum values.
281 Over the Pacific (Fig. S3d), the difference plot between low-ice and high-ice phases is
282 characterized by increased wave fluxes in the troposphere between 35°N and 70°N and in the
283 whole stratosphere which is opposite to the ERA-Interim reanalysis results.

284 This comparison of the planetary-scale EP-fluxes between ERA-Interim and ECHAM6 model
285 results clearly indicates model deficits in the planetary wave propagation characteristics. In
286 particular, the changes in the behavior of the upward propagating planetary-scale waves are of
287 opposite sign in the mid-latitude troposphere over the Atlantic Ocean sector and in the whole
288 troposphere and stratosphere over the Pacific Ocean sector.

289 **4. Conclusions**

290 In accordance with previous studies, [*Cohen et al.*, 2013; *Liu et al.*, 2013; *Kim et al.*, 2014;
291 *Overland and Wang*, 2010; *Francis et al.*, 2009; *Jaiser et al.*, 2012] the presented results
292 support a negative Arctic Oscillation response to observed late summer sea-ice and autumn
293 snow-cover changes on the basis of ERA-Interim reanalysis data. Due to the potential for
294 improved seasonal to inter-annual climate predictions, an in-depth analysis of the
295 performance of global atmospheric models regarding the response to sea ice and snow cover
296 and of possible model deficits is required.

297 Here we showed that the observed negative AO in response to sea-ice and snow-cover
298 changes is underestimated by the AGCM ECHAM6. The planetary wave train structures over
299 the Pacific and North America region are well simulated, but the strengthening and westward
300 shift of the Siberian high pressure system is too weak compared with reanalysis data. We
301 identified deficits in the simulated changes in planetary wave propagation characteristics in
302 response to sea-ice and snow-cover changes, which is one potential contributor to model
303 deficiencies. The changes in the upward propagating planetary-scale waves are of opposite
304 sign in the mid-latitude troposphere over the Atlantic Ocean sector and in the whole
305 troposphere and stratosphere over the Pacific Ocean sector. Our results suggest that
306 improvements in the simulation of the forcing and propagation of planetary-scale waves

307 including troposphere-stratospheric feedbacks are essential for improved seasonal, inter-
308 annual and decadal climate predictions.

309 **Acknowledgements**

310 We thank the data centers of the European center for Medium Range Weather Forecast for
311 providing the ERA-Interim reanalysis (<http://apps.ecmwf.int/datasets>), of the UK Met Office
312 Hadley Centre for providing the HadISST data set (www.metoffice.gov.uk/hadobs/hadisst/),
313 of the Rutgers University for providing the observed monthly snow cover fields
314 (<http://climate.rutgers.edu/measures/snowice/>) and of the National Snow and Ice Data Center
315 for providing the monthly mean sea-ice extent ([ftp://sidads.colorado.edu/DATASETS/NOAA/](ftp://sidads.colorado.edu/DATASETS/NOAA/G02135/Sep/N_09_area.txt)
316 [G02135/Sep/N_09_area.txt](ftp://sidads.colorado.edu/DATASETS/NOAA/G02135/Sep/N_09_area.txt)). We acknowledge the World Climate Research Programme's
317 Working Group on Coupled Modelling, which is responsible for CMIP, and we thank in
318 particular the climate modeling groups at Max Planck Institute for Meteorology Hamburg,
319 Germany and at the German Climate Computing Center (DKRZ), Hamburg, Germany for
320 producing and making available their model output. For CMIP the U.S. Department of
321 Energy's Program for Climate Model Diagnosis and Intercomparison provides coordinating
322 support and led development of software infrastructure in partnership with the Global
323 Organization for Earth System Science Portals. We are particularly grateful to Sabine
324 Erxleben for her support in conducting data analysis and preparing the figures.

325

326

327

328

329 **References:**

- 330 Allen, R. J., and C. S. Zender, (2011), Forcing of the Arctic Oscillation by Eurasian snow
331 cover, *J. Clim.* 24, 6528–6539, DOI: 10.1175/2011JCLI4157.1.
- 332 Blackmon, M. L., and N.-C. Lau, (1980), Regional Characteristics of the Northern
333 Hemisphere Wintertime Circulation: A Comparison of the Simulation of a GFDL General
334 Circulation Model with Observations, *J. Atmos. Sci.*, 37, 497–514, DOI: 10.1175/1520-
335 0469(1980)037<0497:RCOTNH>2.0.CO;2.
- 336 Boisvert, L., T. Markus, and T. Vihma (2013), Moisture flux changes and trends for the entire
337 Arctic in 2003-2011 derived from EOS Aqua data. *J. Geophys. Res.*, 118, 5829-5843,
338 DOI:10.1002/jgrc.20414.
- 339 Brown, R. D., and C. Derksen (2013), Is Eurasian October snow cover extent increasing?
340 *Environ. Res. Lett.*, 8, 024006, DOI:10.1088/1748-9326/8/2/024006
- 341 Cohen, J., M. Barlow, P. J. Kushner, and K. Saito, (2007), Stratosphere-troposphere coupling
342 and links with Eurasian surface variability, *J. Clim.*, 20, 5335-5343, DOI:
343 10.1175/2007JCLI1725.1.
- 344 Cohen, J., J. Furtado, J. M. Barlow, V. Alexeev, and J. Cherry, (2012), Arctic warming,
345 increasing snow cover and widespread boreal winter cooling, *Environ. Res. Lett.* 7,
346 014007, DOI: 10.1088/1748-9326/7/1/014007.
- 347 Cohen, J., J. Jones, J. C. Furtado, and E. Tziperman, (2013), Warm Arctic, cold continents: A
348 common pattern related to Arctic sea ice melt, snow advance, and extreme winter weather,
349 *Polar Oceanogr.*, 26, 152-160.
- 350 Cohen, J., J. A. Screen, J. C. Furtado, M. Barlow, D. Whittleston, D. Coumou, J. Francis, K.
351 Dethloff, D. Entekhabi, J. Overland, and J. Jones, (2014), Recent Arctic amplification and
352 extreme mid-latitude weather, *Nature Geosci.*, 7, 627-637, DOI: 10.1038/NNGEO2234.
- 353 Dee, D. P., S. M. Uppala, A. J. Simmons, P. Berrisford, P. Poli, S. Kobayashi, U. Andrae, M.
354 A. Balmaseda, G. Balsamo, P. Bauer, P. Bechtold, A. C. M. Beljaars, L. van de Berg, J.
355 Bidlot, N. Bormann, C. Delsol, R. Dragani, M. Fuentes, A. J. Geer, L. Haimberger, S. B.
356 Healy, H. Hersbach, E. V. Holm, L. Isaksen, P. Kallberg, M. Koehler, M. Matricardi, A.
357 P. McNally, B. M. Monge-Sanz, J.-J. Morcrette, B.-K. Park, C. Peubey, P. de Rosnay, C.
358 Tavolato, J.-N. Thepaut, and F. Vitart, (2011), The ERA-Interimreanalysis: configuration
359 and performance of the data assimilation system, *Q. J. R. Meteorol. Soc.*, 137, 553–597,
360 DOI: 10.1002/qj.828.

361 Fetterer, F. and K. Knowles, (2004), Sea ice index monitors polar ice extent, *Eos: Trans.*
362 *Americ. Geophys. Soc.*, 85, 163, DOI: 10.1029/2004EO160007.

363 Francis, J. A., W. Chan, D. J. Leathers, J. R. Miller, and D. E. Veron, (2009), Winter Northern
364 Hemisphere weather patterns remember summer Arctic sea-ice extent. *Geophys. Res.*
365 *Lett.*, 36, L07503, DOI: 10.1029/2009GL037274.

366 Ghatak, D., A. Frei, G. Gong, J. Stroeve, and J. Robinson, (2010), On the emergence of an
367 Arctic amplification signal in terrestrial Arctic snow extent, *J. Geophys. Res.*, 115,
368 D24105, DOI: 10.1029/2010JD014007.

369 Honda, M., J. Inoue, and S. Yamane, (2009), Influence of low Arctic sea-ice minima on
370 anomalously cold Eurasian winters. *Geophys. Res. Lett.*, 36, L08707, DOI:
371 10.1029/2008GL037079.

372 Hurrell, J. W., J. J. Hack, D. Shea, J. M. Caron, and J. A. Rosinski, (2008), A new surface
373 temperature and sea ice boundary dataset for the community atmosphere model, *J. Clim.*,
374 21, 5145-5153, DOI: 10.1175/2008JCLI2292.1.

375 Jaiser, R., K. Dethloff, D. Handorf, A. Rinke, and J. Cohen, (2012), Planetary- and synoptic-
376 scale feedbacks between tropospheric and sea ice cover changes in the Arctic, *Tellus* 64A,
377 11595, DOI: 10.3402/tellusa.v64i0.11595.

378 Jaiser, R., K. Dethloff and D. Handorf, (2013), Stratospheric response to Arctic sea ice retreat
379 and associated planetary wave propagation changes, *Tellus*, 65A, 19375, DOI:
380 10.3402/tellusa.v65i0.19375.

381 Kim, B. M., S. W. Son, S. K. Min, J. H. Jeong, S. J. Kim, X. Zhang, T. Shim, and J. H. Yoon,
382 (2014), Weakening of the stratospheric polar vortex by Arctic sea-ice loss, *Nature*
383 *communications*, 5, 4646, DOI: 10.1038/ncomms5646.

384 Kwok, R. and D. A. Rothrock, (2009), Decline in Arctic sea ice thickness from submarine and
385 ICESat records: 1958–2008. *Geophys. Res. Lett.*, 36, L15501, DOI:
386 10.1029/2009GL039035.

387 Liu, J., J. A. Curry, H. Wang, M. Song, and R. Horton, (2012), Impact of declining Arctic sea
388 ice on winter snowfall, *Proc. Natl. Acad. Sci. USA*, 109, 4074–4079, DOI:
389 10.1073/pnas.1114910109.

390 Mori, M., M. Watanabe, H. Shiogama, J. Inoue, and M. Kimoto, (2014), Robust Arctic sea-
391 ice influence on the frequent Eurasian cold winters in past decades, *Nature Geosci.*, 7,
392 869-873, DOI: 10.1038/NGEO2277.

393 Orsolini, Y., R. Senan, R. Benestad, and A. Melsom, (2012), Autumn atmospheric response to
394 the 2007 low Arctic sea ice extent in coupled ocean-atmosphere hindcasts, *Clim. Dyn.*, 38,
395 2437-2448, DOI: 10.1007/s00382-011-1169-z.

396 Overland, J. E. and M. Wang, (2010), Large-scale atmospheric circulation changes are
397 associated with the recent loss of Arctic sea ice, *Tellus*, 62A, 1-9, DOI: 10.1111/j.1600-
398 0870.2009.00421.x.

399 Overland, J. E., K. R. Wood, and M. Wang, (2011), Warm Arctic–cold continents: Impacts of
400 the newly open Arctic Sea, *Polar Res.*, 30, 15787, DOI: 10.3402/polar.v30i0.15787.

401 Park, H., J. E. Walsh, Y. Kim, T. Nakai, and T. Ohata, (2013), The role of declining Arctic
402 sea ice in recent decreasing terrestrial Arctic snow depths, *Polar Sci.*, 7, 174-187, DOI:
403 <http://dx.doi.org/10.1016/j.polar.2012.10.002>.

404 Rayner, N. A., D. E. Parker, E. B. Horton, C. K. Folland, L. V. Alexander, D. P. Rowell, E. C.
405 Kent, and A. Kaplan, (2003), Global analyses of sea surface temperature, sea ice, and
406 night marine air temperature since the late nineteenth century, *J. Geophys. Res.*, 108,
407 D144407, DOI: 10.1029/2002JD002670.

408 Robinson, D. A., K. F. Dewey, and R. R. Heim, (1993), Global snow cover monitoring: An
409 update, *Bull. Am. Meteorol. Soc.*, 74, 1689–1696, DOI: 10.1175/1520-
410 0477(1993)074<1689:GSCMAU>2.0.CO;2.

411 Rinke, A., K. Dethloff, W. Dorn, D. Handorf, and J. C. Moore, (2013), Simulated Arctic
412 atmospheric feedbacks associated with late summer sea ice anomalies, *J. Geophys. Res.*,
413 118, 7698-7714, DOI: 10.1002/jgrd.50584

414 Sato, K., J. Inoue, and M. Watanabe (2014), Influence of the Gulf Stream on the Barents Sea
415 ice retreat and Eurasian coldness during early winter, *Environ. Res. Lett.*, 9, 084009.
416 DOI:10.1088/1748-9326/9/8/084009

417 Screen, J. A., and I. Simmonds, (2010): Increasing fall-winter energy loss from the Arctic
418 Ocean and its role in Arctic temperature amplification, *Geophys. Res. Lett.*, 37, L16707,
419 DOI: 10.1029/2010GL044136.

420 Sokolova, E., K. Dethloff, A. Rinke, and A. Benkel, (2007), Planetary and synoptic scale
421 adjustment of the Arctic atmosphere to sea ice cover changes, *Geophys. Res. Lett.*, 34,
422 L17816, DOI: 10.1029/2007GL030218.

423 Stevens, B., M. Giorgetta, M. Esch, T. Mauritsen, T. Crueger, S. Rast, M. Salzmann, H.
424 Schmidt, J. Bader, K. Block, R. Brokopf, I. Fast, S. Kinne, L. Kornblueh, U. Lohmann, R.
425 Pincus, T. Reichler, E. Roeckner, (2013), Atmospheric component of the MPI-M Earth
426 system model: ECHAM6, *JAMES*, 5, 146-172, DOI: 10.1002/jame.20015.

427 Trenberth, K. E., (1986), An assessment of the impact of transient eddies on the zonal flow
428 during a blocking episode using localized Eliassen-Palm flux diagnostics, *J. Atmos. Sci.*,
429 43, 2070-2087, DOI: 10.1175/1520-0469(1986)043<2070:AAOTIO>2.0.CO;2.
430 Taylor, K. E., R. J. Stouffer, and G. A. Meehl, (2012), An overview of CMIP5 and the
431 experiment design, *Bull. Am. Meteorol. Soc.*, 93, 485-498, DOI: 10.1175/BAMS-D-11-
432 00094.1.
433 Vihma, T., (2014), Effects of Arctic sea ice decline on weather and climate: A review, *Surv.*
434 *Geophys.*, 35, 1175-1214, DOI: 10.1007/s10712-014-9284-0.
435 von Storch, H., and F. W. Zwiers, (1999), *Statistical Analysis in Climate Research*,
436 *Cambridge University Press*, 494 pp.

437

438

439 **Additional information**

440 Supplementary figures are provided.

441

442

443

444

445

446

447

448

449

450

451

452

453

454

455

456

457

458

459

460

461 **Figure legends**

462 **Fig. 1:** First pair of coupled patterns obtained by the maximum covariance analysis (MCA) of
463 HadISST1 sea-ice concentration in September with ERA-Interim sea-level pressure (upper
464 row), GPH500 fields (middle row) and GPH50 fields (lower row) in winter (DJF mean) from
465 1979-2012. Column 1 displays the sea-ice concentration anomaly maps (in [%]) as
466 heterogeneous regression maps. Column 2 displays the corresponding anomaly maps for the
467 atmospheric variables as homogeneous regression maps. Thin black contours show the
468 significance of the regressions at the 95% level. Dashed contours show the climatological
469 mean (1980-2012) atmospheric fields of SLP, GPH500 and GPH50 respectively. All data
470 have been linearly detrended before calculating the MCA.

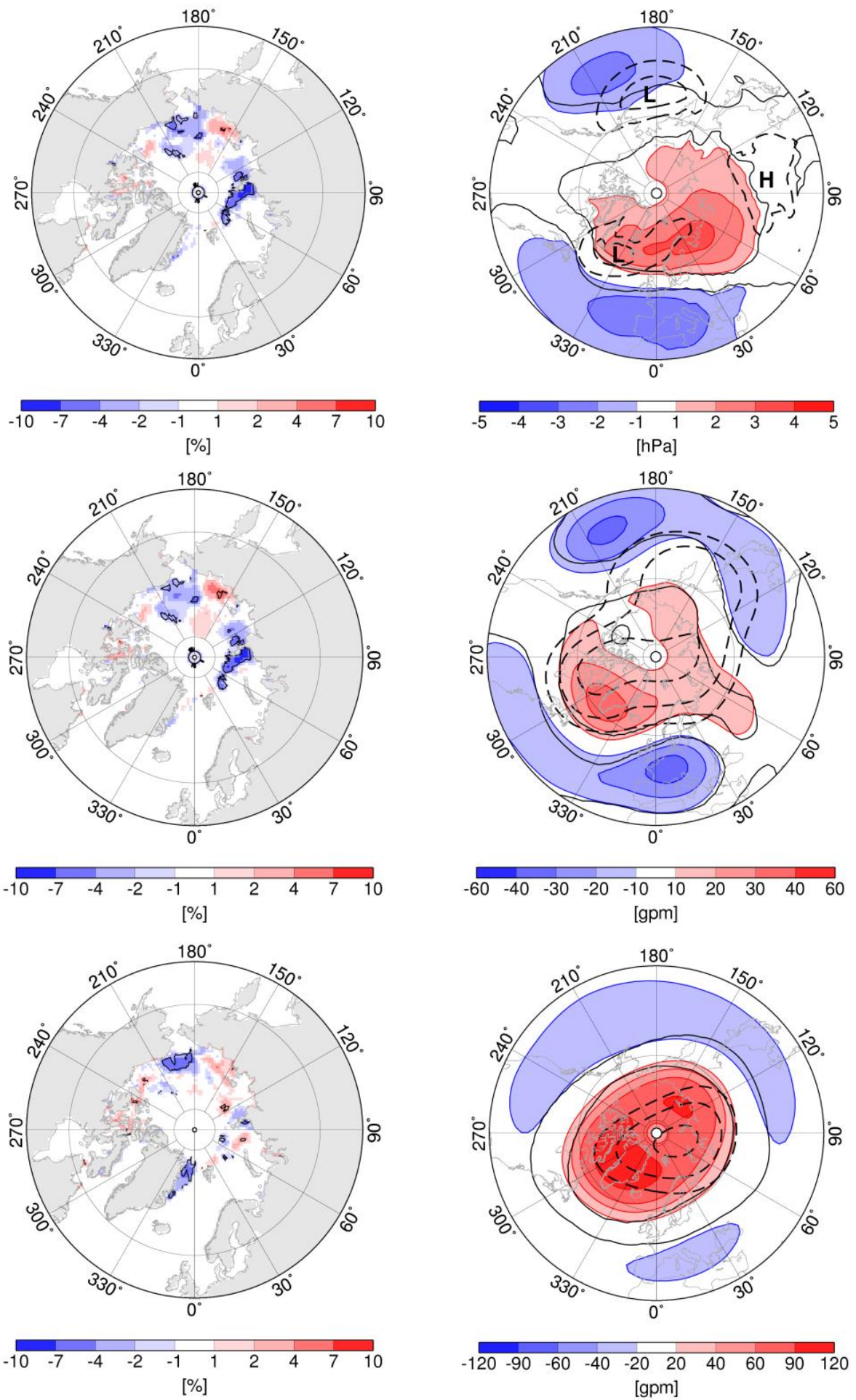
471 **Fig.2:** Second pair of coupled patterns obtained by the maximum covariance analysis (MCA)
472 of HadISST1 sea-ice concentration in September with ERA-Interim sea-level pressure (upper
473 row), GPH500 fields (middle row) and GPH50 fields (lower row) in winter (DJF mean) from
474 1979-2012. Column 1 displays the sea-ice concentration anomaly maps (in [%]) as
475 heterogeneous regression maps. Column 2 displays the corresponding anomaly maps for the
476 atmospheric variables as homogeneous regression maps. Thin black contours show the
477 significance of the regressions at the 95% level. Dashed contours show the climatological
478 mean (1980-2012) atmospheric fields of SLP, GPH500 and GPH50 respectively. All data
479 have been linearly detrended before calculating the MCA.

480 **Fig. 3:** As Fig. 1, but for the first pair of coupled patterns obtained by MCA of HadISST1 sea-
481 ice concentration in September with ECHAM6 model simulated sea-level pressure (upper
482 row), GPH500 fields (middle row) and GPH50 fields (lower row) in winter (DJF mean) from
483 1979-2008. All model data are from the ensemble mean of three ECHAM6-AMIP simulations
484 from 1979-2008.

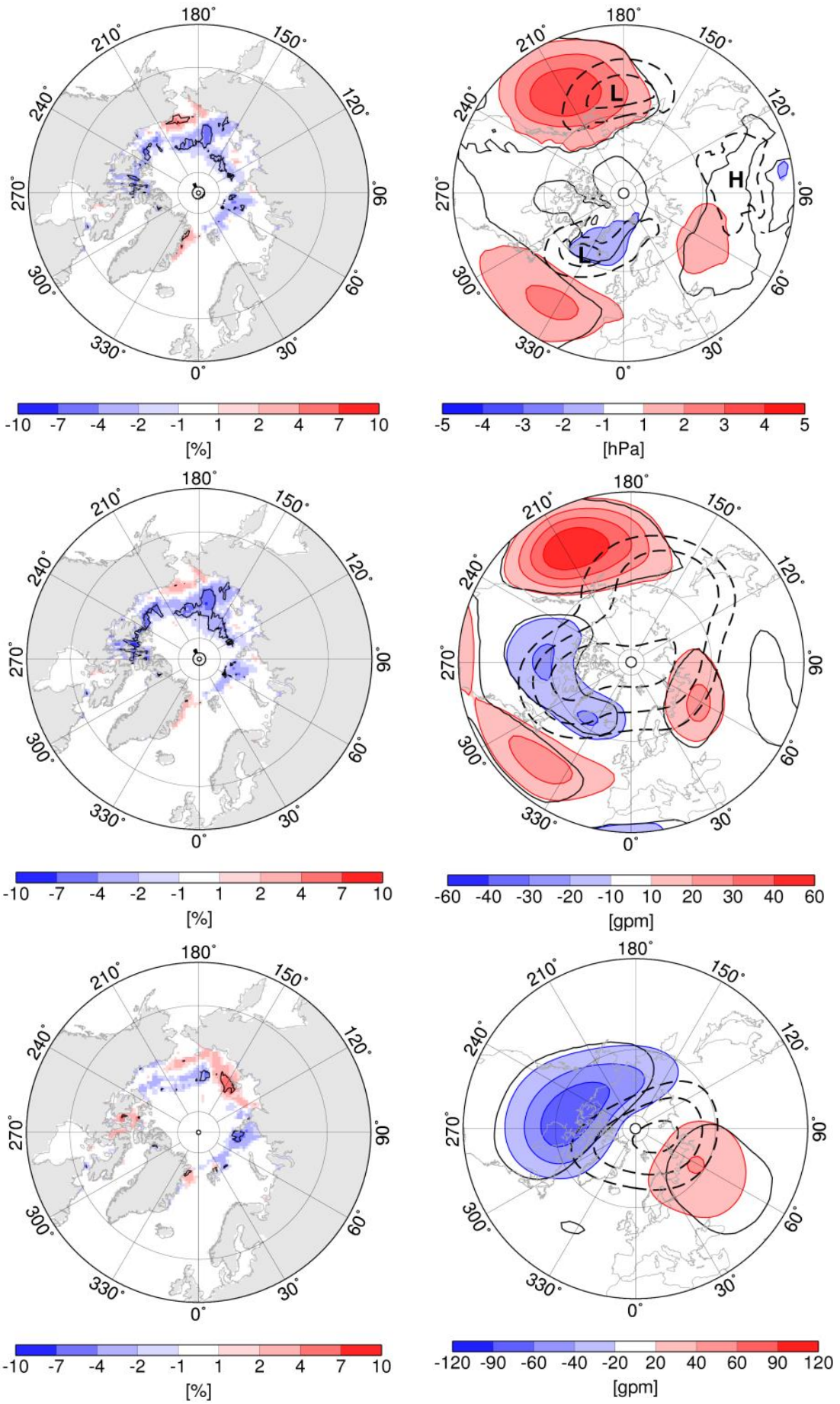
485 **Fig. 4:** As Fig. 1, but for the first pair of coupled patterns obtained by MCA of October snow
486 cover (from Rutgers University snow data set) with ERA-Interim sea-level pressure (upper
487 row) and GPH500 (lower row) in winter (DJF mean) from 1979-2012.

488 **Fig. 5:** (a) Correlation of the zonally averaged magnitude of the planetary-scale wave EP flux
489 vector, calculated for ERA-Interim data for winter (DJF) with preceding September sea-ice
490 index from 1979-2012. Statistical significance with a 90% (95%) confidence level is
491 delineated by dashed (solid) black contour. (b) same as in (a), but correlation of the zonally

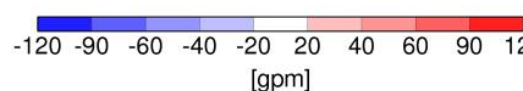
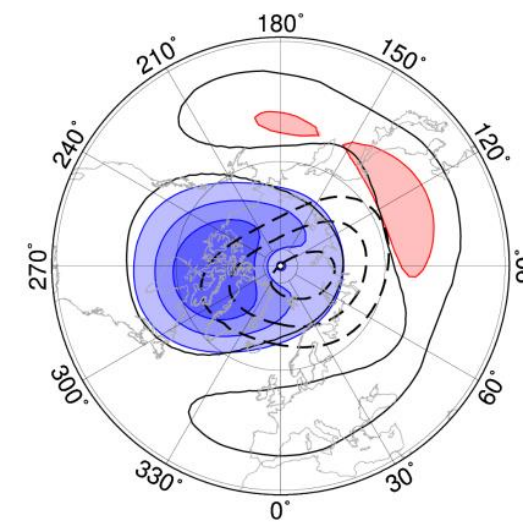
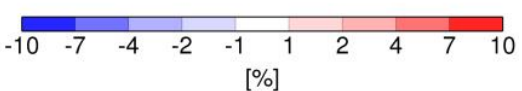
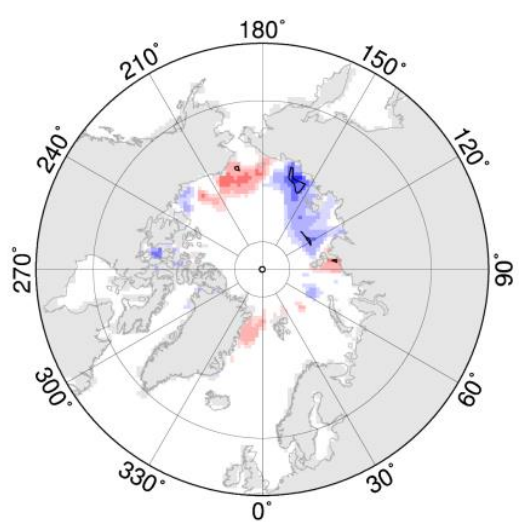
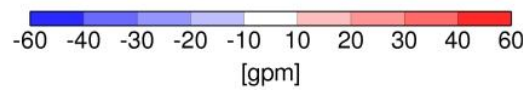
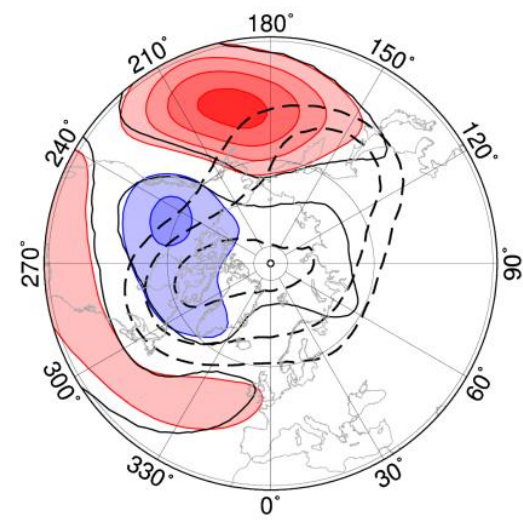
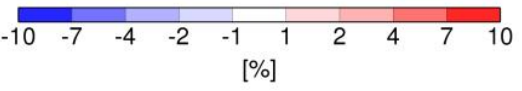
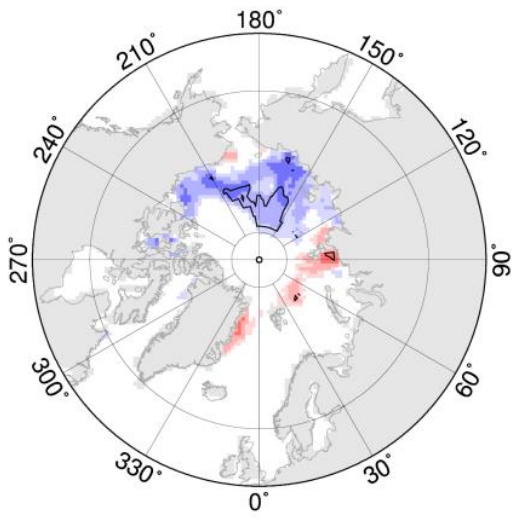
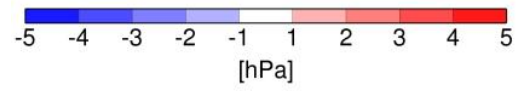
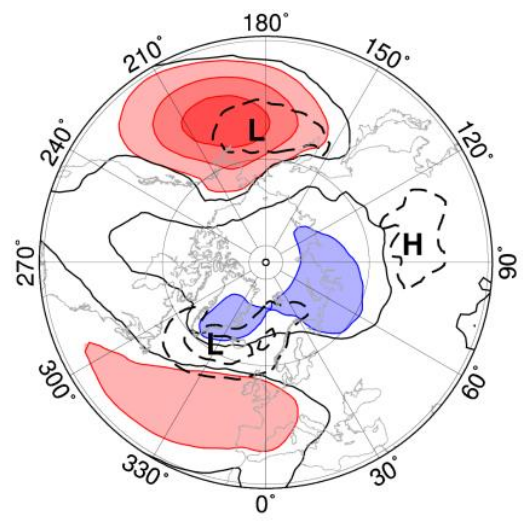
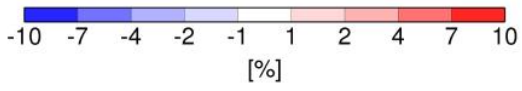
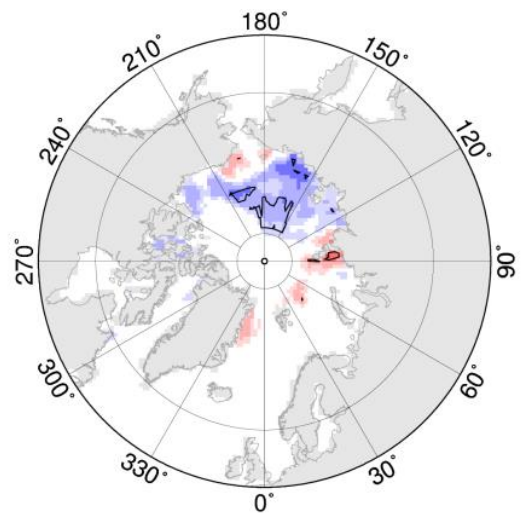
492 averaged magnitude of the planetary-scale wave EP flux vector, calculated for ERA-Interim
493 data for winter (DJF) with preceding October snow-cover index from 1979-2012 (calculated
494 from Rutgers University snow data set). (c) and (d) are the same as in (a) and (b), but the
495 zonally averaged magnitude of the planetary-scale wave EP flux vector and the October
496 snow-cover index for (d) have been calculated for simulated data from the ensemble mean of
497 ECHAM6-AMIP runs from 1979-2008.



498 **Figure 1:**



499 **Figure2:**

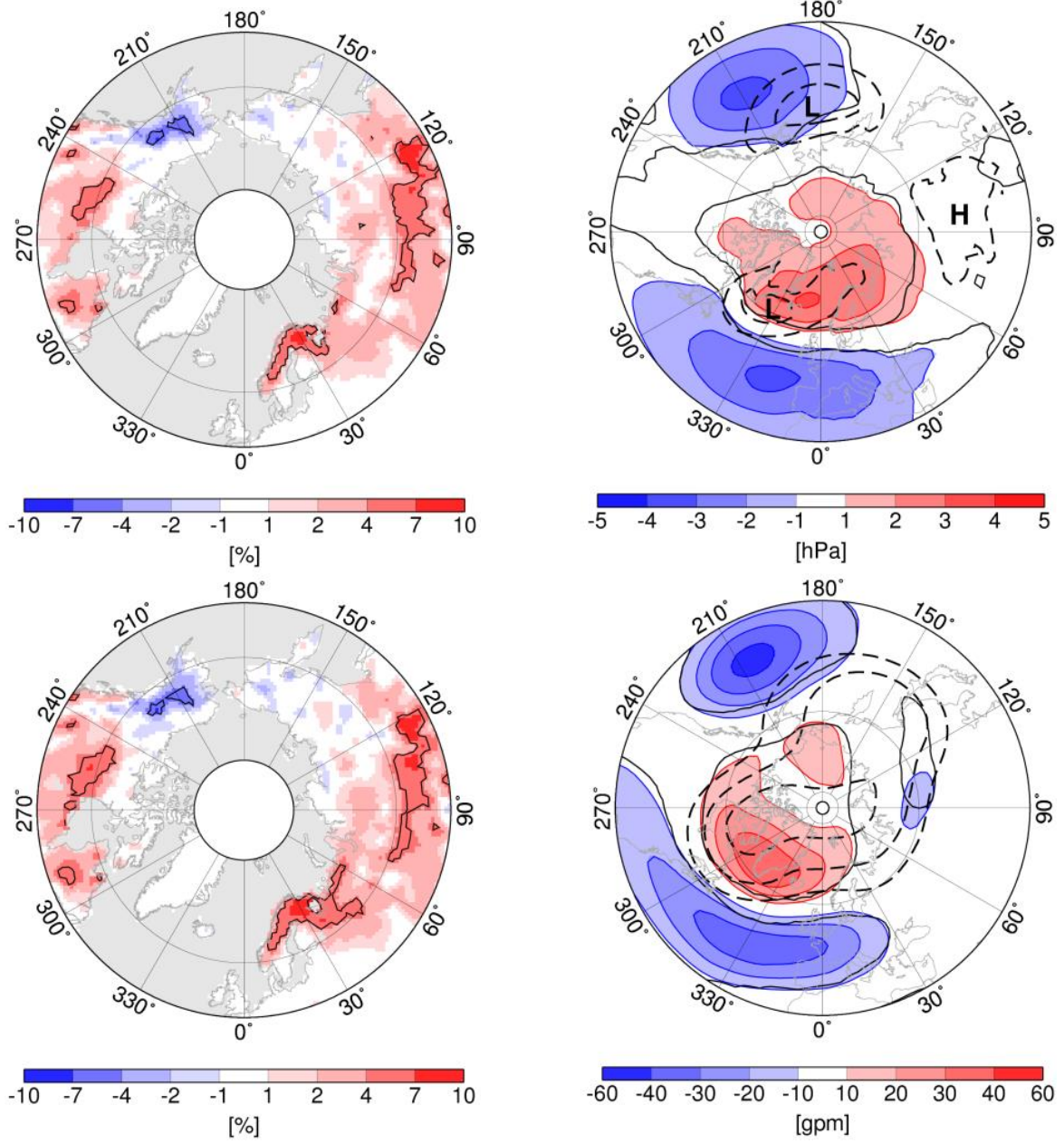


500

501 **Figure 3:**

502

503



504

505 **Figure 4:**

506

507

508

509

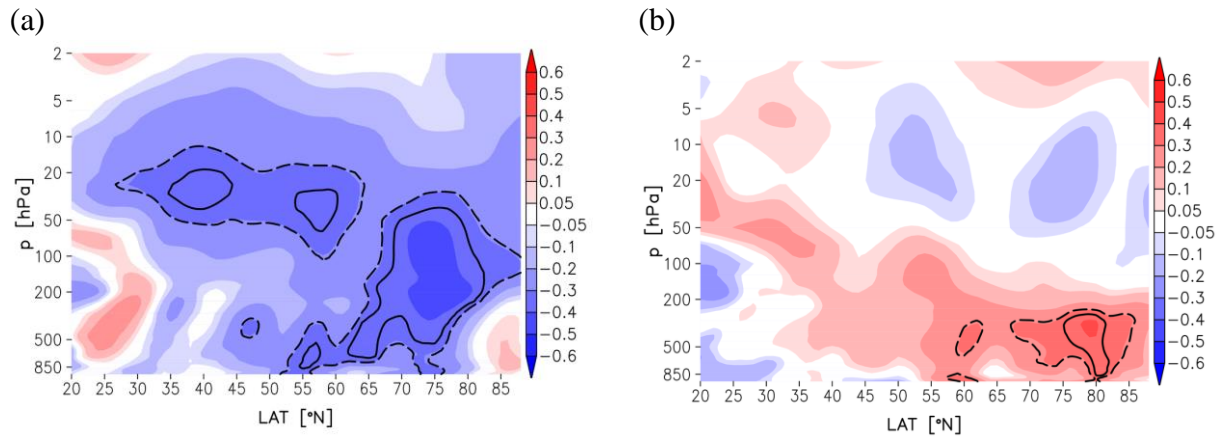
510

511

512

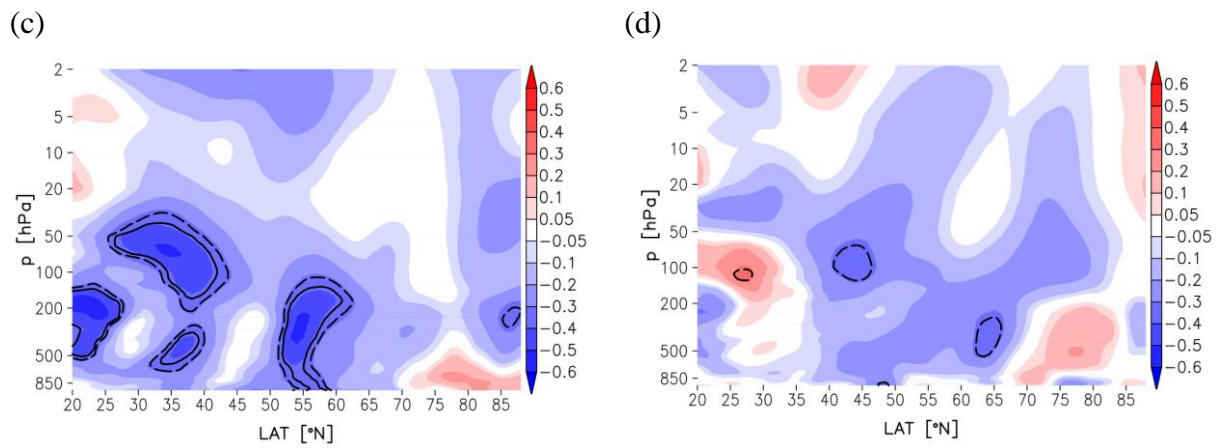
513

514



515

516



517

518 **Figure 5:**

519

520

521

522

523

524